

Installation and characterization of an electron bombardment ion source for a Space Simulation Chamber (SSC)

Karianne Dyrland

FYS-3931 Master's thesis in Space Physics – December 2016

Installation and characterization of an electron
bombardment ion source for a Space Simulation
Chamber (SSC)

Karianne Dyrland

University of Tromsø

December 2016

Abstract

The primary focus of this thesis is the installation and characterization of an electron bombardment ion source for a Space Simulation Chamber (SSC). The goal is that the chamber can be used to test satellite and sounding rocket instrumentation, thus be capable of producing ionospheric plasma conditions, along with an ion beam that can simulate the velocity of a rocket or satellite relative to the atmosphere. The plasma also need to be reproductive.

First, the plasma source was prepared for operation after years in storage. This included changing the filaments and checking the conditions of the electrical connections and magnetic field. A new setup of power sources for the different components was also done.

Second, the source was installed and characterized in the Space Simulation Chamber. Some hang ups were encountered and solved.

Two different electrostatic probes were used to analyse the plasma. A basic Langmuir probe, useful for finding parameters like the plasma potential, electron temperature and plasma density, and a retarding field energy analyzer (RFEA) for finding the ion saturation current and ion energy distribution.

Some inconsistency was found in the plasma potential between the two probes, seemingly indicating the presence of an ion beam. The plasma density is in the order of 10^{11} cm^3 and the electron temperature is in the range 3-5 eV and can be varied using the neutralizing filament.

Acknowledgements

I would like to express my sincerest gratitude to my supervisor Prof. Åshild Fredriksen for all the help and support throughout this project.

I would also like to thank Inge Strømmesen for helping with any technical questions or troubles in the lab, and for developing the Auro Lab Labview systems.

I would like to thank the guys at the University of Tromsø workshop for creating some of my almost impossible inventions.

Further on I would like to thank the Department of Physics and Technology for the possibility to do my masters and working in a brand new lab with the new Space Simulation Chamber.

And lastly I want to thank my family and friends for supporting me in every way possible through all these years at the University of Tromsø.

Contents

Abstract	iii
Acknowledgements	v
Contents	vii
1 Introduction	1
2 Kaufman source	3
2.1 Principles	3
2.1.1 Ion production	4
2.1.2 Discharges	8
2.1.3 Ion extraction, acceleration and neutralization	9
2.2 NDRE plasma source	13
2.2.1 Outer structure and gas inlet	13
2.2.2 Cathode	14
2.2.3 Anode and solenoid	15
2.2.4 Grids and neutralizing filament	16
2.2.5 Storage tank	18
3 Experiment	19
3.1 Preparation	19
3.1.1 Electrical connections	19
3.1.2 Filaments	21
3.1.3 Magnetic flux density	22

3.1.4	Vacuum	24
3.2	Installation	25
3.3	Problems and solutions	27
4	Measurement techniques	35
4.1	Langmuir probe	35
4.1.1	Principles	36
4.1.2	Experimental setup	38
4.2	RFEA probe	40
4.2.1	Principles	40
4.2.2	Experimental setup	42
5	Results and Discussion	45
5.1	Paschen curve	45
5.2	Plasma parameters	46
5.2.1	Plasma potential	47
5.2.2	Electron temperature	50
5.2.3	Ion velocity	52
5.2.4	Ion density	52
5.2.5	Electron density	53
6	Conclusion and future work	55
	Bibliography	57

Chapter 1

Introduction

Since the discovery of the ionosphere in the beginning of the 20th century it has been of great scientific and commercial interest. The conducting layer in our atmosphere bounces radiowaves and made it first possible for us to communicate over long distance. As the second world war started there was a particularly high interest in researching the ionosphere for communication purposes which led to a variety of measurement techniques being developed [1]. The two main categories are ground-based measurements and in-situ ("on-site") measurements. Remote sensing measurements from the ground includes ionosondes, backscatter radars and lidars, while in-situ measurements are done by sounding rockets and satellites carrying probes and plasma instruments [1–3].

In-situ measurements are extremely useful for studying the ionosphere due to their good and accurate data. Space missions are usually very expensive and because rockets and satellites encounter harsh conditions in the lower atmosphere, it is of great interest to be able to test out the rocket and satellite equipment in ionospheric conditions before launching them into space. Thus, a large laboratory environment able to reproduce space plasma parameters along with the velocity of a rocket relative to the ionosphere is needed [4, 5]. In figures 1.1 and 1.2 (figures 4.2 and 4.4 in [1], respectively) the profiles of the electron density and temperature are shown.

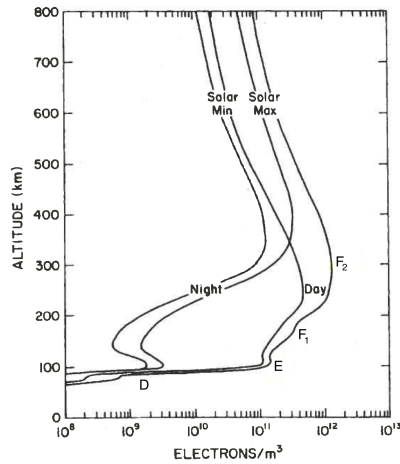


Figure 1.1: Electron density profiles for minimum and maximum sunspot conditions for day and night times (figure 4.2 in [1]).

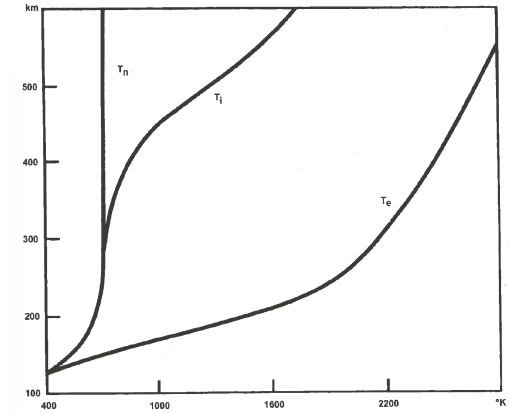


Figure 1.2: Temperature profiles in the ionosphere for electrons, ions and neutrals (figure 4.4 in [1]).

The main goal of this project includes installing and characterizing a plasma source for a Space Simulation Chamber (SSC). The plasma source is an electron bombardment ion source based on the Kaufman source originally designed for spacecraft propulsion, and was originally at the Norwegian Defence Research Establishment (NDRE). The vacuum tank has previously been equipped with an older plasma source that was constructed and described by Hamran in 1984 (see reference [2]). A new plasma source was built by Rein-Heggebakken et al. in 2004 (see reference [6]), based of the old one with several new components intended to improve the source and fix the troubles with the old one. The plasma created in the chamber will also be measured and characterized using electrostatic probes.

Chapter 2

Kaufman source

In this chapter the history and a theoretical description of the Kaufman type plasma source will be given along with a mechanical review of the NDRE plasma source used in this experiment.

The Kaufman source is based on the electrostatic ion rocket engine invented by Kaufman et al. for NASA in the early 1960's. It was the first electric propulsion system that succeeded in-orbit testing through the SERT-I and SERT-II missions and made the way for the Deep Space 1 which was the first of NASA's spacecrafts to use ion propulsion. It was then modified in the 1980's to become the Kaufman type ion source, also known as the electron bombardment ion source [7–11].

2.1 Principles

The Kaufman type plasma source is an electron bombardment plasma source where an electropositive plasma is created through impact ionization between high velocity primary electrons emitted from a glowing filament, and a neutral gas. The filament is the chamber's cathode and is placed in the center of the back wall of a cylindrically shaped plasma source chamber. A current runs through the filament heating it up to emit electrons and it is biased

with a negative voltage V_C with respect to ground. Surrounding the cathode lining the inner and top wall of the cylinder, is the anode which is biased with a positive voltage V_A . The applied voltages on the two electrodes serve to attract their respectively opposite charged particles while repelling the other. In the other end of the chamber, opposite the cathode, a negatively biased grid extract and accelerate the ions out of the source and into a vacuum chamber where the ion beam is neutralized by electrons from a second glowing filament. Electrons emitted from this neutralizing filament mix with the ion beam to produce a quasineutral plasma able to represent the conditions of the ionosphere. See figure ... for a diagram of a basic Kaufman type plasma source [2, 8–10, 12, 13].

INSERT sketch of basic kaufmann source

2.1.1 Ion production

Neutral atoms are ionized through collisions with primary electrons. The primary electrons emitted from the cathode filament are accelerated through the surrounding negative sheath acquiring a kinetic energy \mathcal{E}_e equal to the potential difference between the cathode and the plasma $\mathcal{E}_e = V_p - V_C$. Since most of the potential energy in the source is focused in the area of the sheath close to the cathode filament, and only a very small potential is needed to carry a discharge current across the plasma, the primary electrons pick up most of the available potential energy in the plasma. This leaves the plasma potential V_p inside the source close to the potential of the anode V_A . V_p will be slightly positive with respect to V_A because the electrons have a much higher velocity than the ions they leave the ions behind as they flow to anode. Thus the plasma charges up with respect to the anode until enough electrons are retained to create an equilibrium in the total flux from the filament to the anode. The primary electron energy is therefore approximately equal to the potential between the cathode and the anode $\mathcal{E}_e \approx V_C - V_A$. Figure 2.1 (figure 3.6 in [2]) shows the radial potential difference between the cathode and the anode [2, 12, 14].

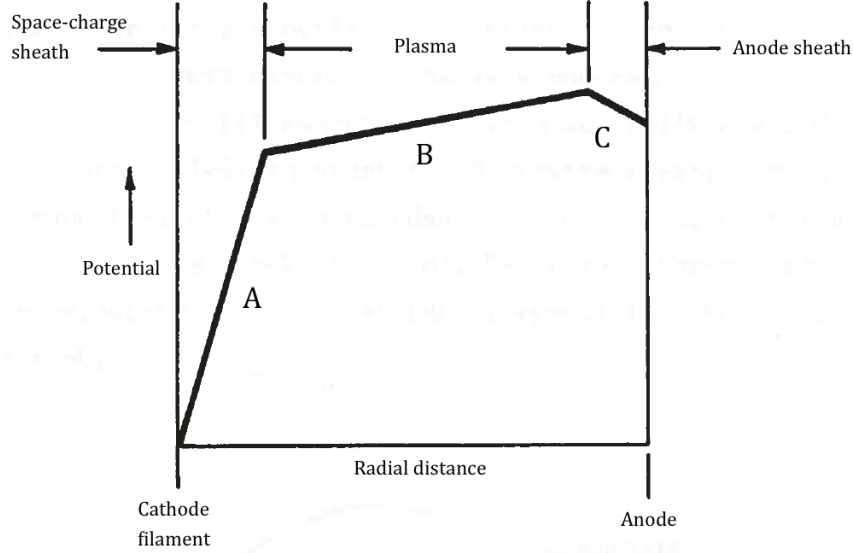


Figure 2.1: Radial plot of potential difference between cathode and anode in plasma source chamber (figure 3.6 in [2])

To be able to ionize a neutral gas atom the primary electrons need to have an electron energy \mathcal{E}_e equal to or greater than the value of the first level ionization energy W_I of that gas species, i.e. the energy needed to remove a valence electron from that atom [12, 14, 15].

$$\mathcal{E}_e \geq W_I \quad (2.1)$$

For Argon we have $W_I = 15.7596 \text{ eV}$ [16].

The condition required for \mathcal{E}_e to be transferred to the valence electron of the neutral atom, assuming a simple classical case, is determined by the ionization or Thomson cross section given by [14].

$$\sigma_{iz} = \begin{cases} \pi \left(\frac{e}{4\pi\epsilon_0} \right)^2 \frac{1}{\mathcal{E}_e} \left(\frac{1}{W_I} - \frac{1}{\mathcal{E}_e} \right) & \mathcal{E}_e \geq W_I \\ 0 & \mathcal{E}_e < W_I \end{cases} \quad (2.2)$$

where e is the elementary charge and ϵ_0 is the permittivity of free space. The Thomson cross section has the unit m^2 .

The ionization or ion production rate is given by [14]

$$\nu_{iz} = n_g \sigma_{iz} v \quad (2.3)$$

where n_g is the neutral gas density and v is the velocity. It is given in the unit ionizations per m^3 per s . Equations (2.2) and (2.3) show that the ion production rate is inversely proportional to the electron energy. For a full treatment of the ionization cross section and ion production rate, see reference [14].

An effective plasma source needs an optimized ion production rate which we can achieve by controlling the paths of the primary electrons. To do this a large coil is wrapped around the anode cylinder creating a solenoid that generates a nearly uniform magnetic field $\mathbf{B} = B_0$ in the axial direction of the chamber. The magnetic field needs to be weak enough so that it only affects the electrons and not the ions in the chamber, i.e. about 50 – 120 G [12, 15]. This makes the electrons gyrate in circular orbits about a guiding center with gyration or cyclotron frequency ω_c and a gyration or Larmor radius r_c . It orbits perpendicular to the magnetic field keeping the electrons contained in the radial direction while the electric field from the potential difference between the cathode and the anode on the inner end of the chamber, and the anode and the negatively biased inner grid on the downstream end, keep them contained in the axial direction. Due to the collisions with the neutral gas atoms the electrons random walk towards the anode with steps approximately equal to the gyration radius, assuming classical diffusion. To make sure each

electron makes on average at least one collision, ionizing at least one neutral atom, the gyroradius should be smaller than half the radius of the anode cylinder r_A [2, 8, 12, 14, 15, 17, 18].

$$r_c < \frac{1}{2}r_A \quad (2.4)$$

The motion of the electrons between collisions can be described by the Lorentz force equation

$$m\frac{d\mathbf{v}}{dt} = q[\mathbf{E}(\mathbf{r}, t) + \mathbf{v} \times \mathbf{B}(\mathbf{r}, t)] \quad (2.5)$$

where m is the particle mass, q is the particle charge, \mathbf{r} and \mathbf{v} are, respectively, the position and velocity vectors, and \mathbf{E} and \mathbf{B} are the electric and magnetic fields, respectively [14, 19].

The gyration or cyclotron frequency of the electron orbits is given by

$$\omega_c = \frac{qB_0}{m} \quad [rad/s] \quad (2.6)$$

and the gyration radius by

$$r_c = \frac{v_\perp}{|\omega_c|} \quad [m] \quad (2.7)$$

where v_\perp is the speed perpendicular to the magnetic field. For electrons, equations (2.6) and (2.7) can be rewritten into more useful units

$$\begin{aligned} f_{c,e} &= \frac{\omega_c}{2\pi} \\ &\approx 2.80 \cdot 10^6 B_0 \quad [Hz] \end{aligned} \quad (2.8)$$

$$r_{c,e} \approx \frac{3.37\sqrt{\mathcal{E}}}{B_0} \quad [cm] \quad (2.9)$$

where \mathcal{E} is the electron energy in electronvolts and B_0 is in the unit gauss [2, 12, 14, 15, 19]. See reference [14] for a full evaluation of the electron motion and the derivation of the gyrofrequency and the gyroradius.

As we can see from equation (2.9) the gyration radius of the electrons in the chamber is proportional to the electron velocity and hence the ionization rate is inversely proportional to the magnetic field strength B . The value of B can be found for an ideal case through Ampere's law [6]

$$B = 10^4 \mu_0 \frac{N \cdot I_c}{l_c} \quad [G] \quad (2.10)$$

where $\mu_0 = 4\pi \cdot 10^{-7} \frac{V \cdot s}{A \cdot s}$ is the permeability of free space, N is the number of windings of the coil, I_c is the electric current running through the coil and l_c is the length of the coil. We use the unit gauss instead of the SI-unit tesla for practical reasons of consistency.

2.1.2 Discharges

As the electrons move through the plasma from the cathode to the anode an electric current arises. When the electrical field between the cathode and the anode is relatively low, this current consist of the primary electrons and becomes saturated when all the available electrons in the source chamber are flowing to the anode. The saturation current typically has a value of picoamperes or nanoamperes. However, if the potential difference between the two electrodes is increased, it eventually reaches a breakdown voltage, V_b , high enough to supply the the electrons created in the ion production with enough with enough energy to ionize at least one neutral atom. This leads to an electron avalanche, i.e. a chain reaction of ionizations, and the current will rise exponentially; this electrical breakdown is known as the Townsend discharge [12, 15, 20–22].

The Townsend discharge is a part of the regime of dark discharges that occur in low pressure plasmas and can be desribed by the first and second

Townsend ionization coefficients, α and γ respectively. The first predicts the number of ionizations one electron makes in one meter while the second describes the probability that a hot ion colliding with the cathode produces a secondary electron [15, 20, 23].

The first coefficient α is defined by [20]

$$\alpha = Ap \exp\left(-\frac{Bpd}{V_b}\right) \quad (2.11)$$

where A and B are experimentally determined constants and are dependent on saturation ionization and ionization energies respectively. p is the pressure, d is the effective distance between the electrodes and $V_b = Ed$ is the breakdown potential.

The second coefficient B is defined by Townsend's breakdown criterion

Rearranging equation (2.11) gives the breakdown potential [14]

$$V_b = \frac{Bpd}{\ln(Apd) - \ln\left(\ln\left(1 + \frac{1}{\gamma}\right)\right)} \quad (2.12)$$

This is known as Paschen's law and gives the breakdown voltage needed to start a discharge in a gas of a specific species. Plotting V_b as a function of pd gives the Paschen curve; a theoretical representation for several types of gases can be seen in figure 2.2 (figure from [24]).

2.1.3 Ion extraction, acceleration and neutralization

In the downstream end of the chamber there is an isolated double-gridded hole in the anode disc. This aperture has the purpose of extracting, accelerating and collimating an ion beam from the plasma source. The ion beam is then neutralized by a second glowing filament electrode mounted on the outside of the source.

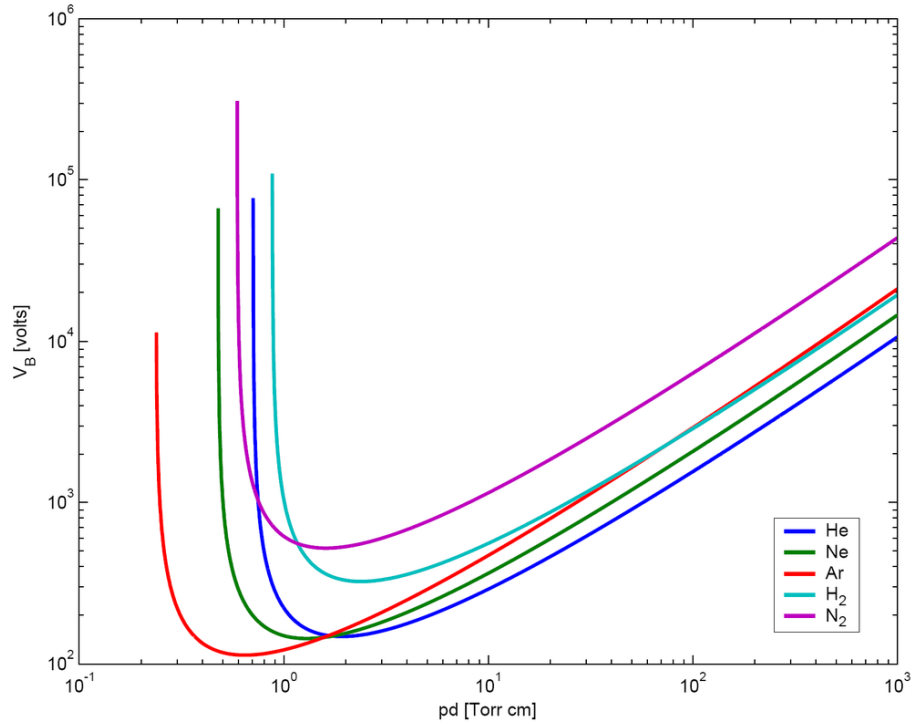


Figure 2.2: A theoretical Paschen curve for several types of gas species (figure from [24], data from [14])

The anode disc with its positive potential, equal to the anode potential of the cylinder wall V_A , works as a screen to stop the electrons from entering the grid system. Highly mobile electrons gather and form a sheath where the potential is set a little lower than the plasma due to the higher electron density. Ions from the more positively charged bulk plasma are attracted to this lower potential and pulled in. On the other side of the sheath is the inner grid, biased with a high negative potential V_{IG} . The ions are pulled towards this potential and accelerated to high velocity through the grid. The acceleration of the ions is given from the potential difference between the anode disc and the inner grid, also known as the acceleration potential [2, 6, 12, 18]

$$V_0 = V_A - V_{IG} \quad (2.13)$$

The outer grid is known as a deceleration grid and is held at a voltage slightly above the ground potential V_{OG} to create a negative sheath. It has the purpose of focusing the ion beam through deceleration. It also prevents the backwards flow of cold ions created by charge exchange with neutrals in the downstream end which can cause abrasion on the accelerator grid [6, 18, 25, 26].

The ion current we are able to extract from the source is limited by both the ion saturation current through the sheath and the space-charge limited current flowing through the grid aperture. The ion saturation current is defined by Bohm's sheath criterion. This explains that the ions must have a given velocity v_B , the Bohm velocity, to pass through the sheath, assuming a collision-less regime. If not the sheath potential will stretch out into the plasma to set up a potential drop able to accelerate the ions up to the required velocity v_B . This is known as the presheath and is typically much wider than the actual sheath [2, 12, 14, 15, 18].

The Bohm velocity is given by [14]

$$v_B = \left(\frac{eT_e}{m_i} \right)^{1/2} \quad (2.14)$$

where e is the electron charge, T_e is the electron temperature and m_i is the ion mass.

The ion current density is given by [14].

$$J_B = en_s v_B \quad (2.15)$$

where n_s is the density at the sheath edge.

Using the electrostatic Boltzmann relation, the sheath density to bulk plasma density ratio is found to be [14, 15]

$$\begin{aligned}
n_s &= n_0 e^{-V_p/T_e} \\
&= n_0 e^{-1/2} \\
&\approx 0.61 n_0
\end{aligned} \tag{2.16}$$

where n_0 is the density at the edge between the bulk plasma and the presheath and V_p is the plasma potential.

The space separating the inner and outer grid is exclusively made up of ions. The ion current density flowing through the grids is limited by space-charge saturation and is governed by the Child-Langmuir law [14]

$$J_0 = \frac{4}{9} \epsilon_0 \left(\frac{2e}{m_i} \right)^{1/2} \frac{V_0^{3/2}}{d_g^2} \tag{2.17}$$

where d_g is the distance between the two grids. We can clearly see that the ion current density is strongly dependent on the potential difference and the spacing between the two grids. We typically want a large acceleration potential and a short separation distance [12, 18, 25].

After exiting the grids the ion beam is neutralized by a glowing filament electrode stretched across and above the outer grid. One side of the filament is held at approximately the ground potential. The ion beam mix with low energy electrons emitted from the neutralizing filament through electrostatic forces and we get a quasineutral beam. Without the imposed neutralization the ion beam would still obtain a partial neutralization by attracting electrons from the surroundings. However the benefits of neutralizing the flux directly is reducing beam divergence and prevent the build-up of large space charge potentials [8, 18, 25, 27].

2.2 NDRE plasma source

In this section a brief mechanical description of the new plasma source and its components will be given. A more detailed review is given by Rein-Heggebakken et al who constructed the plasma source in collaboration with the ionospheric team at the Norwegian Defence Research Establishment (NDRE) [6] and in the project paper reviewing the plasma source by Dyrlund [28]. In figure 2.3 (from figure 7.1 in [6]) we see the main components of the source.

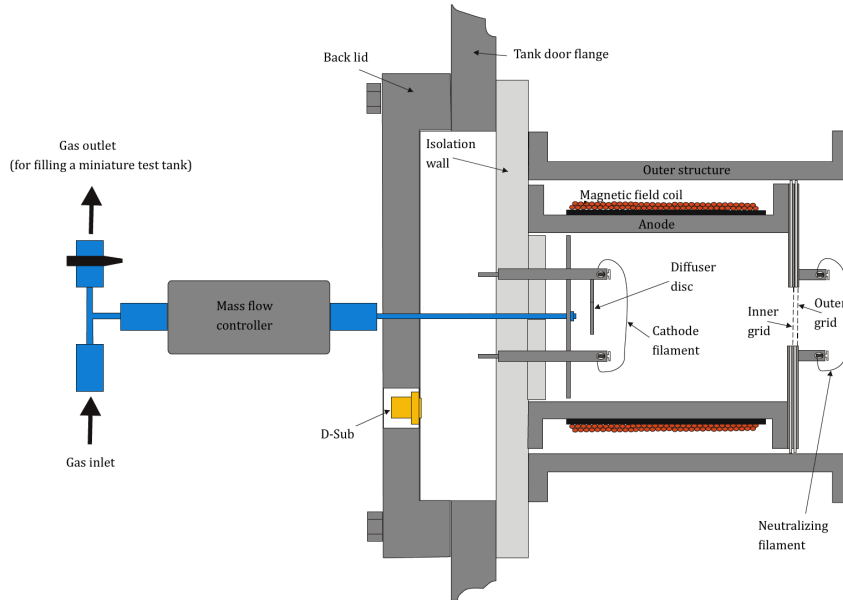


Figure 2.3: The plasma source and the main components (based on figure 7.1 in [6]).

2.2.1 Outer structure and gas inlet

The plasma source is a cylinder of stainless steel with the outer length and diameter $l_{outer} = 185 \text{ mm}$ and $d_{outer} = 135 \text{ mm}$ respectively. On the outside it has an outer structure, a back lid and a top lid both sealed to the cylinder

with O-rings. The outer structure is one of the new components added to this redesign of the plasma source and its function is to provide a pure electric potential in the vacuum chamber and help focusing the ions after they exit the plasma source. On the back lid there is a terminal with wires connected to every component of the plasma source and a gas inlet with a mount for the gas controller. The plasma source uses the noble gas Argon as a propellant, it has several benefits including a low first level ionization energy $W_I = 15.7596 \text{ eV}$, a relatively large cross section and it is cheap and easy to get access to. A tube leads the gas through the back lid and a 20 mm thick isolation wall, and into the inner chamber of the plasma source where it hits a diffuser disc spreading it evenly through the chamber [6, 16].

INSERT pic of back lid

2.2.2 Cathode

In the inner cylinder of the source we have the cathode and the anode. The cathode is a tantalum filament with a diameter $d_f = 0.25 \text{ mm}$ drawn in an arc around the gas inlet and the diffuser disc, and is held in place by two mounts or holders. One of the mounts is in electrical contact with the back wall and the diffuser disc while the other one is isolated so a current can run through the filament. The whole cathode unit consists of the components listed in table ... and can be seen in figures 2.4 and 2.5 (figures 7.20 and 7.23 in reference [6], respectively).

Cathode components	Color code in fig. 2.4
Cathode filament	Navy blue
Filament mounts	Silver
Diffuser disc	Green
Gas tube	Pink
Back wall	Red
Isolation/fastening wall	Light blue
Isolation	Yellow

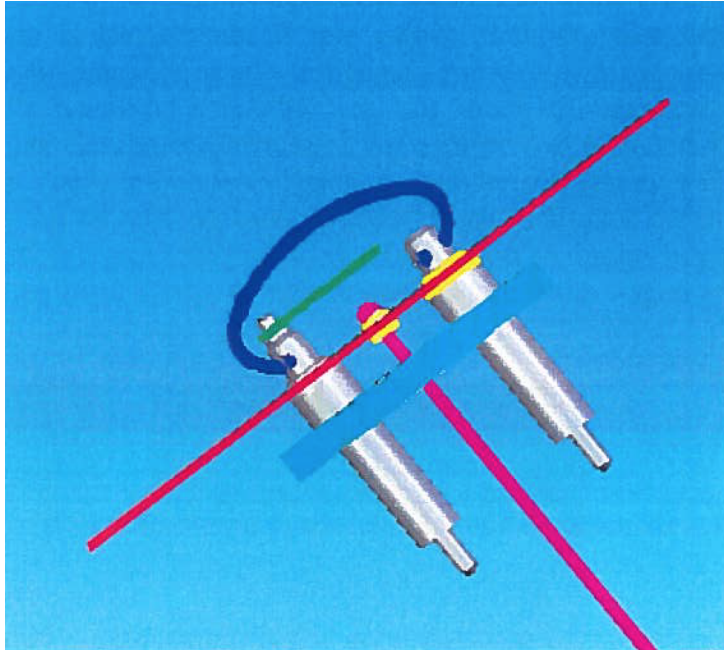


Figure 2.4: Schematic of the cathode filament and components (figure 7.20 in [6])

All components are made of stainless steel except for the fastening plate that is made of the isolating plastic material PEEK, and the filament itself. The cathode unit was designed to be taken out as a whole so the filament can be replaced easily.

2.2.3 Anode and solenoid

The anode is the surface of the inner cylinder wall and a disc in the downstream end of the chamber; they are in electrical contact with each other to keep them both biased at the same potential. The cylinder is made out of stainless steel and has the inner diameter $d_A = 116 \text{ mm}$ and length $l_A = 185 \text{ mm}$. The anode disc is $h_{disc} = 1 \text{ mm}$ thick, it has a diameter $d_{disc} = 132 \text{ mm}$ with a hole with diameter $d_G = 30 \text{ mm}$ in the middle where the grid is located.

INSERT anode disc

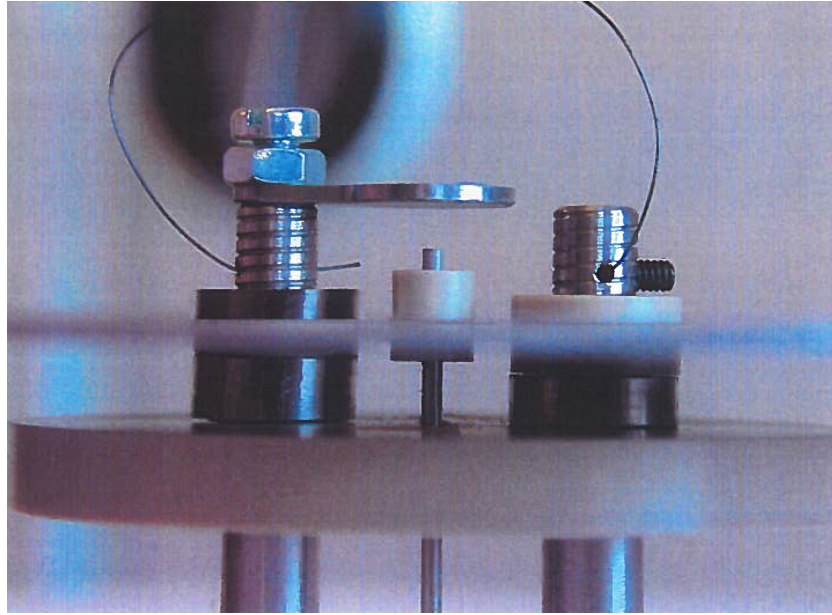


Figure 2.5: Picture of the cathode filament and the components (figure 7.23 in [6])

Between the inner and outer cylinder surrounding the anode is an enameled 1.12 mm thick copper wire forming a solenoid, as seen in figure 2.6 (figure 7.3 in reference [6]). A current is running through it to create a magnetic field inside the plasma source chamber. The solenoid has $N = 410$ windings distributed in three layers, a total length $l_S \approx 160 \text{ mm}$ and an inner diameter $d_S = 121 \text{ mm}$. See section 3.1.3 for a characterization of the magnetic field delivered by the solenoid.

2.2.4 Grids and neutralizing filament

This plasma source has a double grid, where the outer grid is a new feature added together with the outer structure. The inner grid is isolated from the anode with a disc of the isolating material PVC, as the inner grid is going to have a large negative voltage applied to it there will be a high potential difference between these components and no electrical contact can be present. Another PVC disc is on the other side of the inner grid, separating

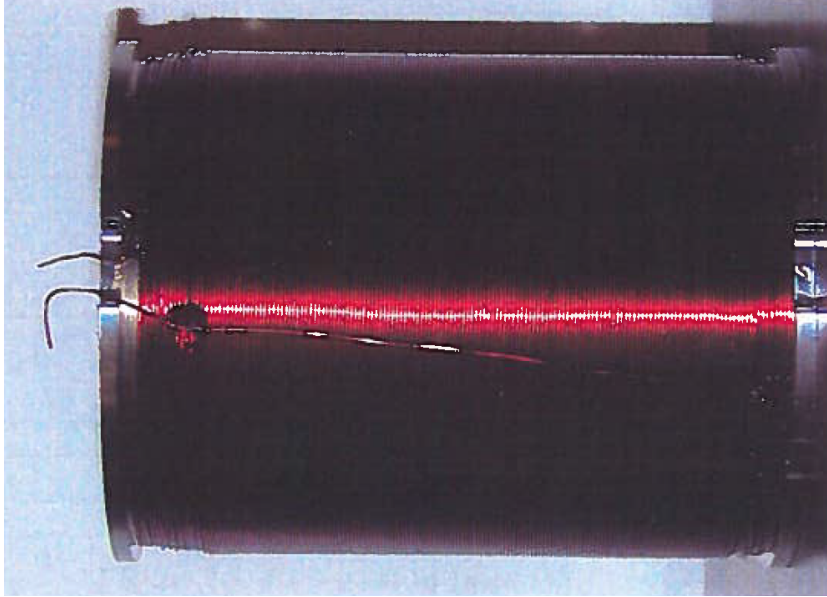


Figure 2.6: Plasma chamber with surrounding solenoid (figure 7.3 in reference [6])

it from the outer grid that is on the outside top lid of the plasma source. The outer grid is positively biased and has the function of grabbing high energy primary electrons that has managed to escape through the inner grid, as this was a problem with the old source where they would interfere with the neutral plasma wanted in the vacuum chamber. Both grid discs have a diameter $d_{disc} = 132 \text{ mm}$ and are made out of stainless steel with a circular grid in the middle with a diameter $d_G = 30 \text{ mm}$. The grid holes have a $d_h = 0.5 \text{ mm}$ diameter and distributed with a 0.5 mm distance between them. The isolating discs have a circular 30 mm hole in the middle equal to the anode disc, all grid and isolating discs are $h_{disc} = 1 \text{ mm}$ thick.

To get a neutral plasma electrons are added to the ion beam exiting through the grids by a neutralizing filament stretched in a straight line across the top of the outer grid. The filament is of the same type as the cathode filament, a Tantalum thread with a diameter $d_f = 0.25 \text{ mm}$ and is held in place by two mounts and is raised approximately 10 mm above the outer grid.

2.2.5 Storage tank

The last new addition to the source was a small miniature tank and sealing lid. This makes it possible to test the plasma source with all components operating without it being connected to the large vacuum tank. It is also useful for storage purposes; when the source was stored for longer periods exposed to air the filaments would start oxidizing and it would contaminate the source under the next operation, however with the new miniature tank it is possible to store it with a gas, sealed from the outside environment.

INSERT pic of mini tank

For more on the troubles of the old source, and both proposed and added solutions, see references [2, 6, 29].

Chapter 3

Experiment

In this chapter the process of preparing, installing and configuring the NDRE plasma source to the Space Simulation Chamber will be reviewed, along with the hang ups and problems solved underway (for a mechanical review of the source, see section 2.2).

3.1 Preparation

The plasma source had been in storage since it was constructed in 2004 so a thorough check of the source had to be done before it was ready to be installed. Wires and other parts also had to be equipped to fit our needs.

3.1.1 Electrical connections

After a decade in storage a test of the electrical system was needed to make sure all the components still had contact with their respective outputs. The condition of the filaments also had to be checked. To reach all the different parts of the source and the filaments, the source had to be disassembled. The front containing the neutralizing filament and the grids was first screwed off to get access to the anode and cathode filament, then the back lid was taken

off to reach the solenoid. This needs to be done with great care as the gas tube is attached to the back wall and goes into a hole in the isolation wall that it needs to be pulled carefully out of in a horizontal direction so it does not bend.

To test the electrical connections a multimeter was used to check every components to their respective output in the terminal block. The tables in appendices 1, 3 and 4: *Elektriske tilkoblinger*, *Koblingsliste D-Sub* and *Rekkeklemmetabell* in Rein-Heggebakken was used as a guide during the tests. All the connections were in working as they should, and in the right place respective to the table.

The plasma source did not come with the connector for the terminal block and a new one had to be ordered along with the wires and plugs needed to make a wire connected to each output on the terminal leading to a current or voltage source. The connector arrived first and while waiting for the wires and plugs, a couple of temporary wires were used to connect a current source to solenoid to perform a test of the magnetic field in the chamber using a gaussmeter with an axial probe, see section 3.1.3 for results and analysis of this. After receiving the wires and plugs they had to be connected to the terminal connector. The source components have ten outputs in total, hence ten wires had to be prepared. Eight of the wires have the dimensions $A_{w,1} = 1 \text{ mm}^2$ while two have the dimensions $A_{w,2} = 1.5 \text{ mm}^2$, this is related to how much current can run through them, a good rule of thumb is that a 1 mm^2 wire will take a current up to about 10 A while a 1.5 mm^2 wire will take up to about 15 A and so on. While it would have worked with the smaller ones on all the components as none need currents higher than 10 A , thicker ones were used on the solenoid so there was a possibility to go higher if ever that is needed. Metal tips were then crimped onto one end of all the wires and screws tighten them into place on the connector terminal block. Banana plugs were connected to the other end on all the smaller wires and lugs to the two larger ones, as they were leading to a larger power supply without any banana plug inputs. See section 3.2 for a review of the power supplies used for the source.

3.1.2 Filaments

The filaments already installed in the source were thin and old, and had to be replaced before installation. This was done while waiting for the terminal connector block and the wires (see section 3.1.1). As mentioned in section 2.2.2 the whole cathode unit was designed to be taken out as a whole with a pair of long screws that fit into ridged holes next to the cathode filament. However it did not work to pull it out of the cylinder as described and we resorted to opening the source up from the back by removing the isolation wall to prevent damaging any of the components as it was not clear how it was fastened on the back.



Figure 3.1: The disassembled plasma source as the cathode filament is being changed

The filament thread used in the source is made of tantalum and would be preferred, but unfortunately we did not have any tantalum filament available in the lab and it needed to be ordered. This could take a couple of weeks to arrive and to prevent too much delay we decided to use a tungsten filament instead as it is a very common filament used in other plasma sources. While waiting for the tantalum filament we would then be able to install and run preliminary tests on the source, and change to the tantalum one when the

tungsten filament needed to be replaced as glowing filaments do not have a very long lifetime. Hamran explains in reference [2] some problems encountered while using a tungsten filament due to the fact that tungsten emits electrons at a higher temperature and more power is needed to run it, so some heating in the source could be expected. However, the experiment did not call for operation over a longer period of time so we expected it would not be a large problem for testing the basic functions of the source, as it should still work as normal with a tungsten filament. The filament mounted inside the anode cylinder can be seen in figure 3.2.



Figure 3.2: View inside the anode cylinder and plasma source, where the cathode filament is stretched horizontally across the diffuser disc in the middle.

After the filaments was replaced the isolation wall and back lid was reattached.

3.1.3 Magnetic flux density

While the source was disassembled the magnetic field generated by the solenoid inside the source was tested. A gaussmeter (NOTE type) with axial probe was used to test the magnetic field strength. The probe was mounted on a

stand and placed approximately in the middle of, and parallel to the source chamber, as seen in figure 3.3.



Figure 3.3: The axial probe of a gaussmeter is installed on a mount to test the magnetic field strength, produced by the solenoid, inside the plasma source.

The magnetic field strength or magnetic flux density B was measured at a set of predetermined values for the current running through the solenoid I_c to get a relationship between the current and the magnetic field. We have from equation (2.10) that the magnetic field strength is proportional to the current so we would expect a near linear increase in field strength as the current increases. The results can be seen in figure 3.4. A theoretical evaluation was also done using equation (2.10) and is plotted next to the measured values.

As we see in figure 3.4 the theoretical values and the measured values coincide well, within $\pm 10 G$ at the most. For lower values the theoretical curve and the experimental curve are very close, $\pm 2 G$, and the curves diverge as the current values increases. The results also fit relatively well with the test previously done by Rein-Heggebakken et al [6] seen as the yellow plot. As the solenoid heats up the ohmic resistance in the wire increases, which is most likely the cause for the divergence of the theoretical and experimental values.

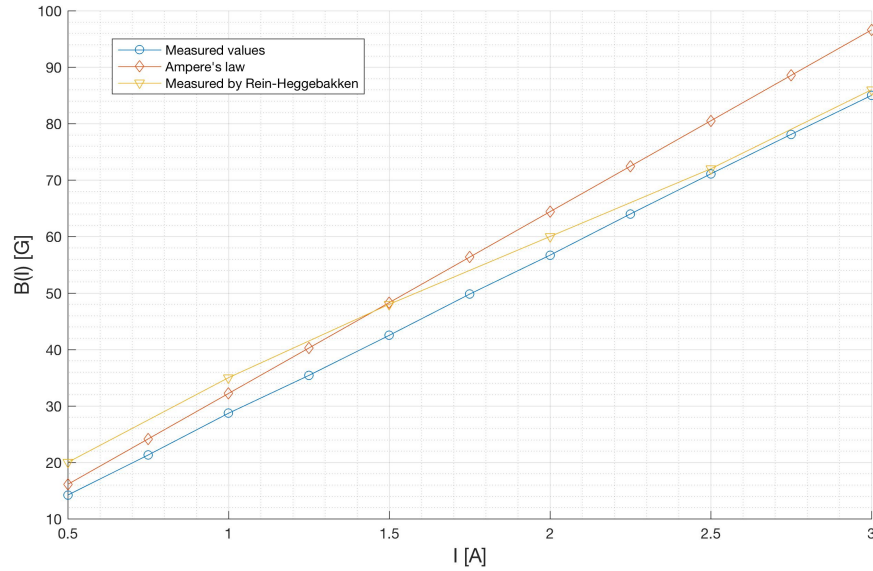


Figure 3.4: The magnetic field strength in the plasma source chamber. Blue are the measured values and red are theoretically calculated values using eq. (2.10). Yellow is measurements made by Rein-Heggebakken et al, values are from figure 7.7 in [6].

3.1.4 Vacuum

Before the source is installed a test of the vacuum system was done.

The vacuum chamber has the dimensions $l_v = 2.16 \text{ m}$ times $d_v = 0.96 \text{ m}$ [30]. The volume can easily be calculated to

$$\begin{aligned}
 V &= \pi r^2 l_v \\
 &= \pi \left(\frac{d}{2}\right)^2 \cdot l_v \\
 &= 1.5634 \text{ m}^3
 \end{aligned} \tag{3.1}$$

It is equipped contains a roughing pump and two turbo pumps of the type HiPace 800 each backed up by a Pfeiffe Penta 350 rotary vane pump. It was first tested with one turbo pump and was able to maintain a pressure of $p =$

$1.2 \cdot 10^{-5}$ *mbar* after about a week, which is relatively good for a chamber this large. When the second turbo pump of the same type was also connected the pumping time decreased remarkably and was able to pump down to a pressure of $1.2 \cdot 10^{-5}$ *mbar* in about 7-8 hours. A pressure as low as 10^{-6} *mbar* would be preferred but this is relatively close to the ionospheric values we are looking for and in general good enough for laboratory experiments [2, 30].

Before installing the plasma source we configured the vacuum tank to fit our needs and installed a large window on the far end, directly opposite the source. We also installed a smaller one on the side of the chamber, closer to the source. These are useful for having a visual contact with the filaments in the source.

3.2 Installation

The plasma source was mounted in the front door of the vacuum chamber and a mass flow controller for the argon gas was attached on the back. When the source was constructed, a custom Labview program was written by Rein-Heggebakken et al [6] to control the gas flow to the source and was hooked up to the source through the terminal on the back of the source with wires that led to a D-Sub connector for the mass flow controller. Auro lab at UiT is already equipped with a good setup and Labview program for the vacuum pumps and the mass flow control, so that was used instead for this experiment. Figures 3.5 and 3.6 show the plasma source installed in the vacuum chamber door. The first is a sideview from the outside of the chamber along with a view of the mass flow control and all wires attached. The latter show the source mounted in the door on the inside of the chamber, along with the outer grid and the neutralizing filament.

All the components in the source is going to be biased at different voltages relative to a reference ground point, the solenoid and the two filaments also need a current running through them, hence several separate power sources are needed. Figure 3.7 (figure 7.32 in [6]) show an overview of the electrical

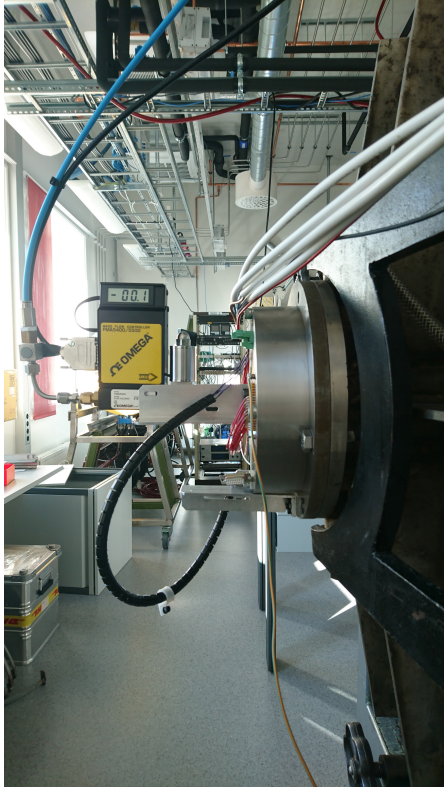


Figure 3.5: Sideview of source mounted on chamber, mass flow controller installed



Figure 3.6: Plasma source installed in SSC. View of neutralizing filament and outer grid

potentials relative to the ground all the different components are biased to during normal operations.

In figure 3.8 all the power sources needed to run the plasma source are shown, the power sources and their designated voltages and currents together with their respective components are listed in table 3.1.

The back lid of the plasma source was chosen as a ground reference point, and a wire was attached to a screw using a lug. A banana plug was attached to the other end to easily connect several sources in a series to the ground point using the same wire. The complete electrical diagram for the source can be seen in figure 3.9 (figure 4.2 in [31]).

The figure shows the structure of the plasma source with all the different

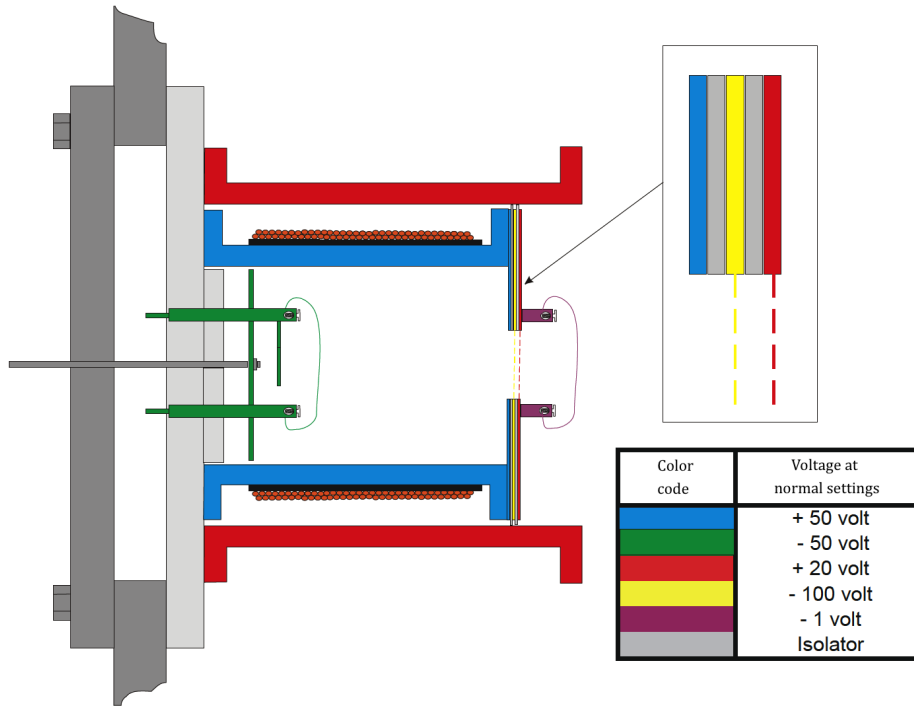


Figure 3.7: The potentials relative to ground applied to the different source components during normal operations (figure 7.32 in [6])

potentials and currents applied to each component, where U_K is the cathode filament current, U_D is the potential applied to the cathode filament, i.e. the discharge potential, U_N is the current for the neutralizing filament and U_A , U_Y , $U_{G,i}$, $U_{G,y}$ are the anode, outer structure, inner grid and outer grid potentials respectively.

In figure 3.10 we see the chamber while in operation, with the glowing filaments and a probe in front of it.

3.3 Problems and solutions

This section will review some of the hang-ups encountered during this experiment along with the implemented solutions.



Figure 3.8: The setup of the different power sources needed to run the plasma chamber (see table 3.1 for details).

After the initial installation, the source was operated and tested a couple of times without troubles. However after some time, an electrical connection happened between the anode, inner grid and outer grid. The source had to be dismantled from the vacuum chamber and disassembled. The problem was that the PVC insulation between the grids had melted and evaporated, leaving a conductive layer of carbon, i.e. soot, on the inside rim of all the grid components. PVC has a melting point of 100 – 260°C and temperatures in the chamber had been too hot for the plastic material, possibly due to the tungsten filament as it emits electrons at a higher temperature than the previously used tantalum filament [2, 32]. To gain access to the grids and insulation the whole grid unit, or top lid of the chamber, had to be taken apart. The PVC with the melted inner rim can be seen in figure 3.11. The best solution would be to completely exchange the PVC discs for ceramic discs, as it is capable of withstanding very high temperatures and

Power source	Source type	Component	Value
Delta Electronika ES 015-10	Current	Cathode filament	2 – 5 A
Delta Electronika ES 015-10	Current	Neutralizing filament	2 – 5 A
Delta Electronika SM 70-AR-24	Current	Solenoid	1 – 2 A
Delta Electronika ES 0300-0.45	Voltage	Cathode filament	–50 V
Delta Electronika ES 075-2	Voltage	Neutralizing filament	–1 V
Delta Electronika ES 0300-0.45	Voltage	Anode	+50 V
Delta Electronika ES 0300-0.45	Voltage	Inner grid	–100 V
Delta Electronika ES 030-05	Voltage	Outer grid	+20 V
Delta Electronika ES 030-05	Voltage	Outer structure	+20 V

Table 3.1: Power source type, designated components and their values for normal operation of the plasma source.

is a common material used in experimental plasma physics. However, the discs need to be 1 *mm* thick and have a diameter $d_{disc} = 132$ *mm*, which is very thin and large for such a fragile material. Also, we had no pieces of ceramic large enough available in the lab to try it. Instead we figured that only the inner rim could be cut out and replaced by a ceramic inner circle, so that the most exposed part of the insulation would be able to stand higher temperatures. I made a sketch and the UiT workshop was able to make it; the final configuration is shown in figure 3.12.

While the top lid was disassembled the screw connecting the inner grid to a wire fell off. It had not been properly fastened as it was just jammed into a hole with no head to stop it on the other side. When the bolt fastening the wire is screwed on, naturally the screw is pulled out and disconnected. In need of a better solution I suggested making a PEEK screw with a very thin head, less than 1 *mm* to make it fit in the space between the inner and outer grid. After drawing a sketch, the workshop managed to construct it. Now the head stops the screw being pulled through the hole and the wire

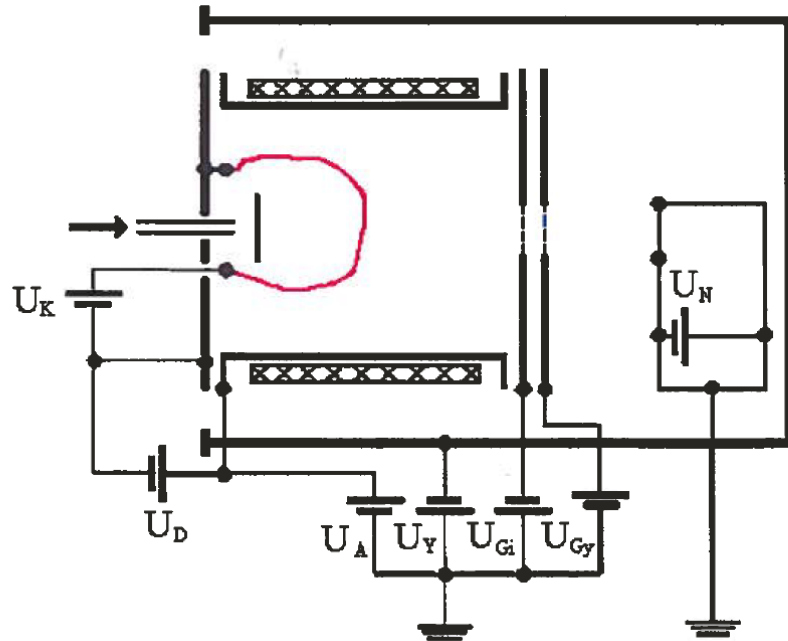


Figure 3.9: Electrical diagram of the plasma source (figure 4.2 in [31]).

connected to the inner grid is properly connected, it can be seen in figure 3.13.

Also seen in figure 3.13 is the insulated wires connecting the grids to their respective power sources. When the lid is opened, e.g. when the filament needs to be changed, the enamel on the wires is very easily scraped off and it also looked like an electrical connection had occurred between these wires due to a layer of soot in the surrounding area. To prevent this from being a problem the wires were insulated separately with a layer of tape.

The cathode filament and the neutralizing filament also had to be replaced three times during the project. Replacing the cathode filament proves to be especially cumbersome and time consuming; the screws holding the filament are very small and is placed awkwardly on the side of the mounts instead of the top as they are for the neutralizing filament.

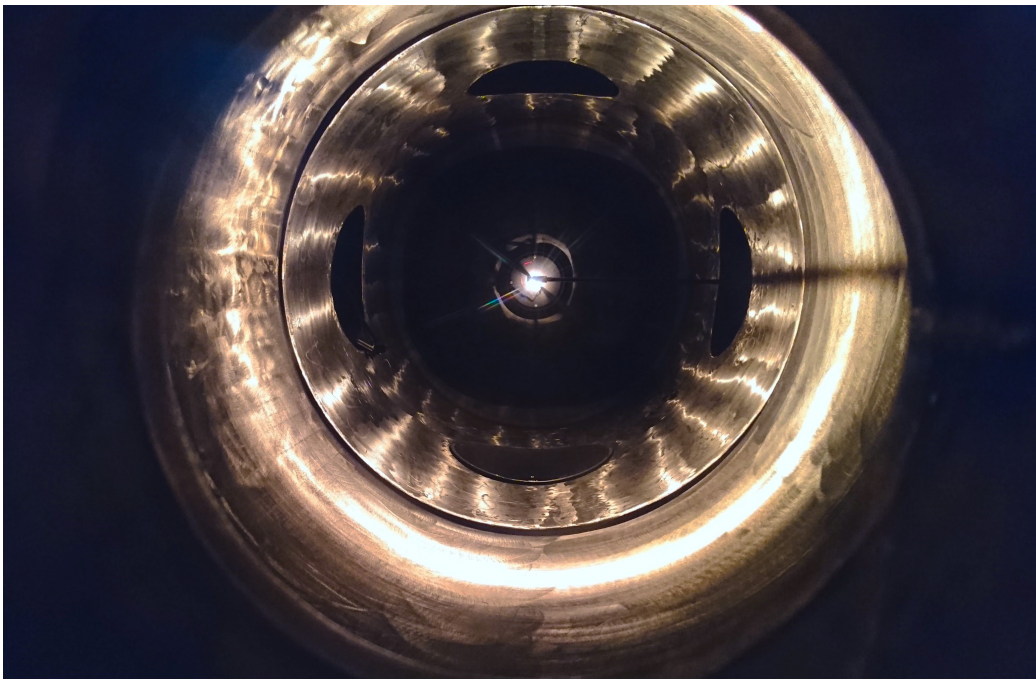


Figure 3.10: The Space Simulation Chamber while operating. The light is from the glowing filaments, and a probe can be seen right in front of it.



Figure 3.11: The PVC insulation separating the grids in the plasma source with a melted inner rim.

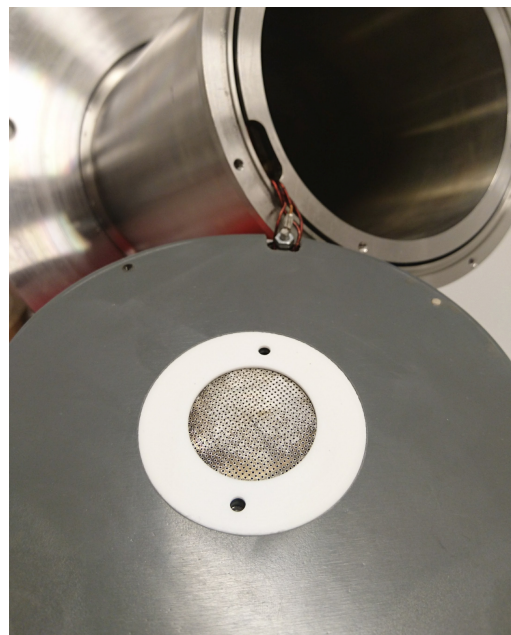


Figure 3.12: The inner part of the PVC insulation is replaced by a ceramic circle so it can handle higher temperatures



Figure 3.13: The inner grid disc with the connecting wire screwed on. Also seen passing through are the two wires for the neutralizing filament and one for the outer grid.

Chapter 4

Measurement techniques

In this section the apparatus and techniques used for characterizing the Space Simulation Chamber and the discharge plasma within are discussed. Definitions and methods for deriving important plasma characteristics, e.g. the plasma potential, the electron temperature and the plasma density, are given.

4.1 Langmuir probe

A simple and effective instrument for measuring the parameters of a plasma is the Langmuir probe. It is named after plasma physics pioneer Irving Langmuir and consists of an electrode biased with a time-dependent potential. The probe is immersed into a plasma and a potential is swepted from highly negative to highly positive voltages relative to the ground, thus attracting the ions and electrons respectively. The electric current $I(V_B)$ is collected as a function of the biased voltage V_B and when plotted it produces what is known as the characteristic current-voltage curve or IV-curve seen in figure 4.1 (from figure 3.6 in [2]). From the IV-curve several plasma parameters can be determined, namely the plasma potential, the floating potential, the electron temperature, the ion velocity, the plasma density [2, 15, 33–35]

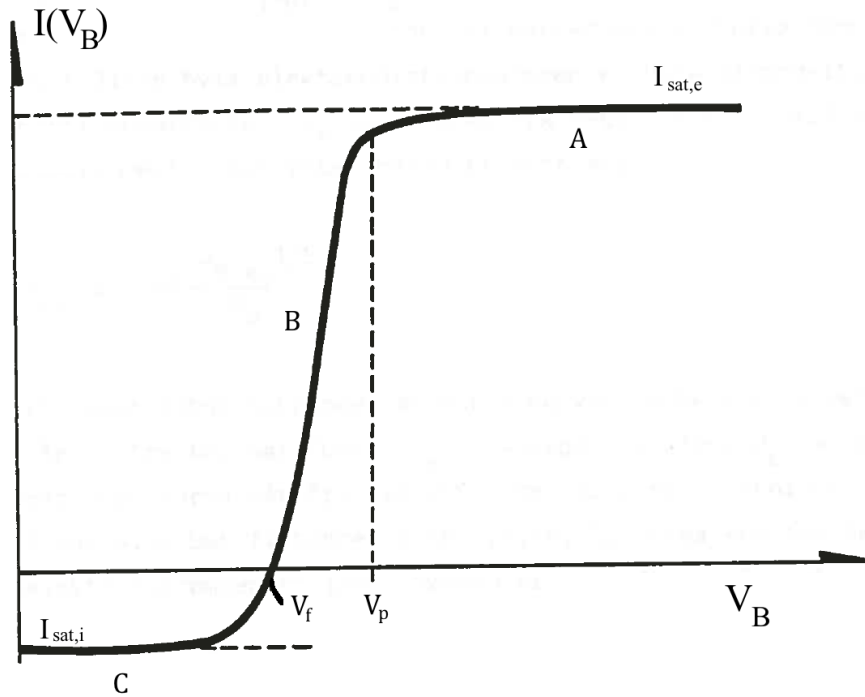


Figure 4.1: A theoretical IV-curve showing the current collected $I(V_B)$ by a Langmuir probe with a time-dependent potential sweep V_B . Region A shows the electron saturation current $I_{sat,e}$, region B is the transition region and region C shows the ion saturation current $I_{sat,i}$. V_p indicates the plasma potential, and V_f is the floating potential (edited from figure 3.6 in [2]).

4.1.1 Principles

Figure 4.1 shows three regions, A, B and C. Region C displays the ion saturation current $I_{sat,i}$, region B shows the transition regime, and region A includes the electron saturation current $I_{sat,e}$. The figure also indicates the plasma potential V_p , and the floating potential V_f defined as the bias potential where the current contribution from the ions and the electrons are equal [14, 33, 34]. The figure includes the ion saturation current $I_{sat,i}$ in region C, the transition regime in region B, and the electron saturation current $I_{sat,e}$ in region A. It also indicates the plasma potential V_p , and the floating potential V_f defined as the bias potential where the current contribution from the ions and the electrons are equal [14, 33, 34].

When the probe is biased with a large negative potential, the ion saturation current is drawn. For a non-magnetized plasma when the probe is biased enough negatively to collect only ions, $I_{sat,i}$ is defined by the Bohm current density J_B , given in equation (2.15), multiplied with the effective collecting area of the probe A_{tot} . If the plasma is magnetized the effective collecting area is that perpendicular to magnetic field lines, meaning for a plane probe only the area of one side is used [14, 33, 36].

The ion saturation current is given by [14]

$$I_{sat,i} = en_i v_B A \quad (4.1)$$

where A is the effective collective area probe, n_i is the ion density and v_B is the Bohm velocity given in equation (2.14).

The ion saturation current can be directly measured from the IV-curve and equation (4.1) can be rearranged to find the ion density at the probe sheath edge [14]

$$n_i = \frac{I_{sat,i}}{ev_B A} \quad (4.2)$$

The plasma density at the sheath edge related to the bulk plasma density by equation (2.16). The Bohm velocity, and hence the density, is determined using the electron temperature T_e .

First an expression for the current in this region is needed. Since the electron saturation current is much higher than the ion saturation current due to their small mass, $I_{sat,i}$ can be neglected, and we obtain [33]

$$I(V_B) = \begin{cases} -Aen_e \left(\frac{k_B T_e}{2m}\right) & V_B \geq V_p \\ -Aen_e \left(\frac{k_B T_e}{2m}\right) \exp\left(\frac{e(V_B - V_p)}{k_B T_e}\right) & V_B < V_p \end{cases} \quad (4.3)$$

Assuming a Maxwellian velocity distribution in the electrons, T_e can be found in the region between the floating potential and the plasma potential, $V_f < V_B < V_p$. Rearrange equation 4.3 to get [33]

$$\frac{d}{dV_B} \ln|I(V_B)| = \frac{e}{k_B T_e} \quad (4.4)$$

Solve for T_e to get

$$T_e = \frac{e}{k_B} \frac{dV_B}{d(\ln|I(V_B)|)} \quad [K] \quad (4.5)$$

where we can use the relation $e/k_B = 11604.25 \text{ K} = 1 \text{ eV}$ to get an expression given in electronvolts

$$T_e = \frac{dV_B}{d(\ln|I(V_B)|)} \quad [eV] \quad (4.6)$$

Plotting the IV-curve with a logarithmic y-axis gives a near linear curve in the area between V_f and V_p , where the electron temperature can be procured directly from the slope.

The floating potential V_f can be found on the curve when $I_{sat,i} = I_{sat,e} = 0$ and is expected to be relatively close to the ground potential when the plasma is surrounded by a large grounded structure, e.g. the vacuum chamber [14].

The plasma potential V_p is defined as the maximum value of the first derivative of the IV-curve and as the zero-point on second derivative. The latter is typically more accurate, but is often difficult to use due to too much noise in the signal.

4.1.2 Experimental setup

A plane probe was built and custom fitted for SSC. A circular piece of conducting metal with a diameter $d_L = 1 \text{ cm}$ was spot welded to the end of a

thin nickel wire. The wire was covered in ceramic insulation all the way up to the probe to keep it from expanding the effective area of the probe. The vacuum chamber thoroughfeed is connected to the side of the chamber about 37 cm away from the probe, measured in a straight line along the center of the chamber. However, we wish to install the probe at about a 10 cm distance from the plasma source, meaning it needs to be brought closer. An L-shaped joint was installed at a distance of about 27 cm from the probe, then a connector was soldered on to the end of the wire and placed inside the joint. The connector can be directly connected to the thoroughfeed pole and placed approximately along the middle axis of the vacuum chamber, as seen in figure 4.2.

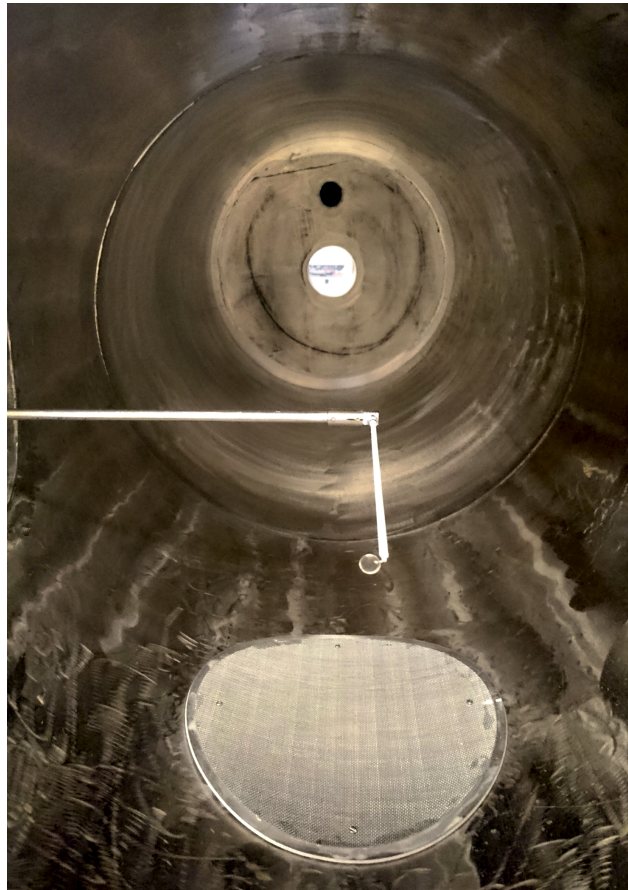


Figure 4.2: The Langmuir probe installed in the Space Simulation Chamber

The probe is controlled using a Labview data acquisition program in Auro lab.

Here, values for the sweep range, number of steps in the sweep and offset are implemented. A battery unit is also connected to this setup and can be used to control the offset in the sweep as well as the program. The distributed signal goes through a sweep amplifier and is then applied to the probe. The current collected by the probe as a function of the sweep voltage is sent back over a resistor, that can be easily changed to control the amplification of the signal, and through an amplifier [33].

4.2 RFEA probe

Another simple and commonly used probe in plasma diagnostics is the retarding field energy analyzer (RFEA). It collects an ion saturation current over a potential sweep, while constantly repelling electrons. The RFEA probe is typically used to find the ion velocity distribution, the ion energy distribution and the ion temperature from a plasma beam [37–40].

4.2.1 Principles

The RFEA probe consists of several small grids placed inside an outer, cylindrically shaped, housing. The housing is usually either a metal structure floating at the ground potential or made of some insulating material, e.g. ceramics, leaving it at the plasma potential; the latter is often preferred as it does not perturb the plasma as much [37]. The front plate of the probe, i.e. the part facing the plasma beam, has a small aperture in the middle, often covered by a grounded grid. Inside there are typically two or three grids, separated by insulated rings, and a collector plate. The first grid is the repeller grid and is biased strongly negative to repel and stop electrons from entering the aperture. The second is the discriminator grid which is biased with a time-dependend sweep V_g from a negative to a positive voltage, similar to that used in the Langmuir probe, however only ions with a parallel kinetic energy higher than V_g are able to pass through. If one chooses to apply a third grid

it is commonly biased positively and used to stop any electrons that may have escaped through the front grid, and to contain the secondary electrons sputtered from the collector as high energy ions collide into it. The collector plate is often applied with a weak negative bias to attract the incoming ions [37, 39].

The probe characteristics of an RFEA produce an IV-curve with an ion saturation current and no electron current. Typical RFEA IV-curves (figure 6 from [38]) can be seen in figure 4.3 for different pressure values).

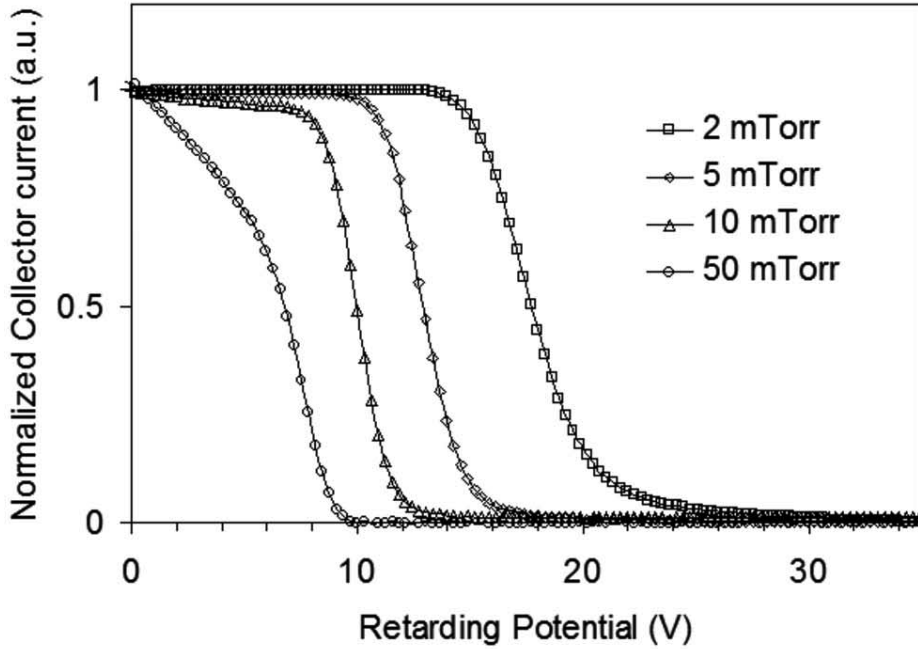


Figure 4.3: Typical IV-curves produced by an RFEA probe for different values of pressure (figure 6 from [38]).

The collected ion saturation current is given by

$$I(v_0) = Ae \int_{v_0}^{\infty} v f(v) dv \quad (4.7)$$

where A is a constant depending on the front plane pin-hole, v is the ion velocity and $f(v)$ is the ion velocity distribution function or the ion energy distribution function. v_0 is the minimum velocity and is given as [37, 39]

$$v_0 = \sqrt{\frac{2eV_g}{m_i}} \quad (4.8)$$

where m_i is the ion mass. From equations (4.7) and (4.8) it is clear that the velocity distribution function is proportional to the derivative of the collected ion current with respect to V_g . Using this we find an expression for the ion velocity distribution function [39]

$$f(v_0) = -\frac{m_i}{Ae^2} \frac{dI(V_g)}{dV_g} \quad (4.9)$$

4.2.2 Experimental setup

The RFEA probe used in this experiment consists of a cylindrical ceramic housing with a front plate, three grids and a collector plate inside. The front plate is made of stainless steel and has an aperture with a diameter $d_{ap} = 4 \text{ mm}$. Behind it is the front grid, which should be grounded but is not connected to anything due to faulty wires in the probe. The probe would work well enough for our purposes without it, so we did not spend time trying to fix this. Then we have the repeller grid, this is applied with a voltage $V_r = 70 \text{ V}$ and is there to repel electrons. The last grid is the discriminator with a time-dependent potential bias applied, similar to the Langmuir probe. The collector gather the ion current of the ions able to pass through the sweeping potential. All grids and the collector are made of stainless steel, and all the grids have a transparency of $T_g \approx 0.5$.

A schematic of the RFEA probe can be seen in figure 4.4 (adapted from figure 3 in [37]). Both the sweep signal and the incoming probe signal go through two separate amplifiers. The collector is biased to $V_{collector} = -9 \text{ V}$ using a battery pack.

The probe is installed in the same way as the Langmuir probe, on the thoroughfeed with an L-shaped joint, however the probe is 10 cm shorter than the Langmuir probe, hence it is placed at a distance at 20 cm away

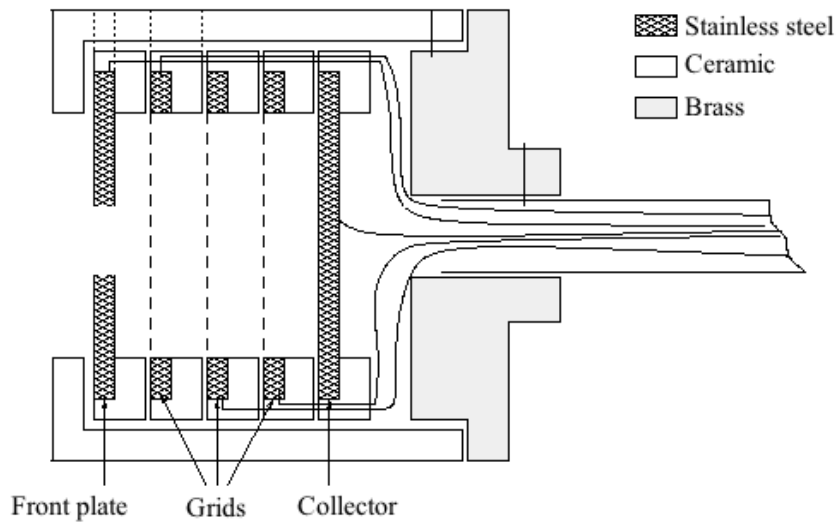


Figure 4.4: Sketch of the RFEA probe with the different components and materials (adapted from figure 3 in [37]).

from the plasma source.

Chapter 5

Results and Discussion

In this chapter the results obtained in the experiment are presented. The plasma parameters are derived and discussed with reference to the theory reviewed in chapters 2 and 4, along with their significance regarding the Space Simulation Chamber (SSC).

5.1 Paschen curve

In equation 2.12 we see the breakdown criteria for a plasma discharge to happen in a specific gas species as a function of pressure. Measurements were taken at different pressures where the voltage needed to make breakdown happen was noted. Two data sets were recorded and can be seen plotted in figure 5.1.

For the x-axis only the pressure p was used instead of the traditional product pd , where d is effective distance between cathode and anode. This is due to the complex geometry of our plasma source, where we have a central cathode and a much larger cylidrically shaped anode. From the results in figure 5.1 we see a curve shaped as expected compared to the theoretical one from figure 2.2.

The plasma is relatively reproductive as seen from the consistency of the

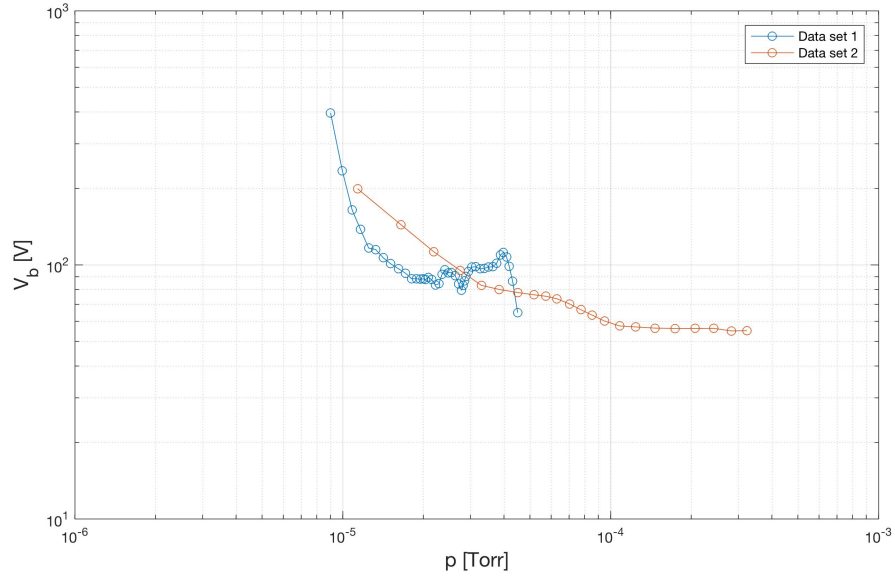


Figure 5.1: Two sets of experimentally measured values for the Paschen curve for an argon gas discharge in the ion source. A moving average filter and a Savitzky-Golay filter has been applied to the curves for smoothing.

two data sets, which is a major goal in building a Space Simulation Chamber. A few things to note is that when breakdown happens the discharge grows exponentially, and since the values for the breakdown voltage are being manually adjusted and recorded the measurements of V_b should have an error of about $\pm 5 V$. The pressure sensors has an estimated error of about $\pm 0.5 \cdot 10^{-5} \text{ mbar}$.

5.2 Plasma parameters

The Langmuir probe and the retarding field analyzer (RFEA) probe are both used to determine the plasma parameters for the plasma created by the ion source. Both probes produce a characteristic IV-curve from which most parameters can be derived from. A set of IV-curves from the Langmuir probe, where the plasma source is set to the voltage parameters for normal operation given by figure 3.7, a neutralizer current $I_N = 3.6 A$ and a pressure

$p = 3.5 \cdot 10^{-5} \text{ mbar}$, is found in figure 5.2.

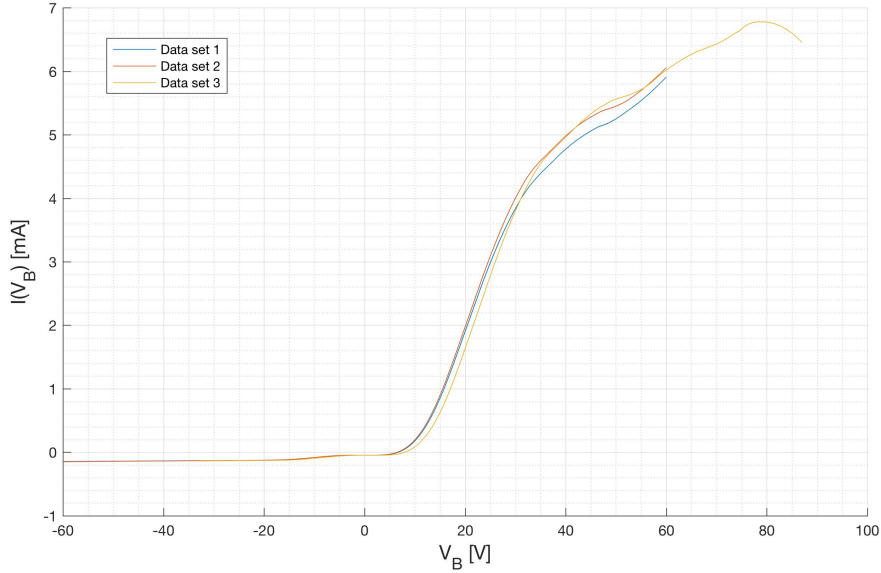


Figure 5.2: IV-characteristics from Langmuir probe measured at parameters for normal operation of the plasma source, with $p = 3.5 \cdot 10^{-5} \text{ mbar}$ and $I_N = 3.6 \text{ A}$.

The Langmuir IV-curves for constant parameters are very similar, supporting that the plasma is reproducible. Compared to the theoretical Langmuir IV-curve from figure 4.1 we see that the electron saturation current keep rising instead of flattening out; this is due to the fact that increasing bias voltage also increases the effective collection area of the probe and is expected [14].

5.2.1 Plasma potential

The plasma potential V_p can be found through derivatives of the IV-curves. In the first derivative, the plasma potential is defined as the maximum value while in the second derivative it is defined as the zero-point value. The latter is usually more accurate, but harder to obtain due to very noisy second derivatives.

In figure 5.4 the first derivatives of the Langmuir IV-curves from figure 5.2

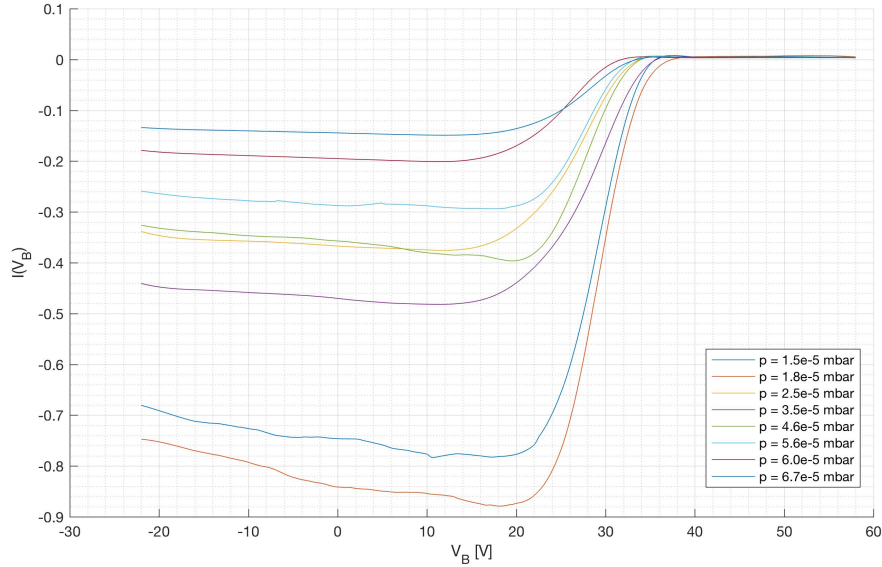


Figure 5.3: IV-curves from RFEA probe measured at normal voltage parameters (see figure 3.7) at different values for pressure

can be seen and the first derivatives of the RFEA IV-curves seen in 5.3 are plotted in figure 5.5. The plasma potential found from the maximum on each curve is listed in table 5.1. We can typically say that the error is within $\pm T_e [eV] n$ [33].

Probe	Data set name	V_p
Langmuir	Data set 1	20.4 V
Langmuir	Data set 2	20.4 V
Langmuir	Data set 3	22.2 V
RFEA	p = 2.5e-5 mbar	28.13 V
RFEA	p = 6.0e-5 mbar	26.53 V

Table 5.1: The plasma potential values obtained from the first derivative IV-curves from the Langmuir and the RFEA probe, see figures 5.4 and 5.5.

As mentioned in section 4.2.2 the rfea probe is placed twice as far away from the plasma source than the Langmuir probe, hence the plasma potential should decrease with distance. However, according to our measurements seen in table 5.1 it does not. A probable explanation is that the RFEA

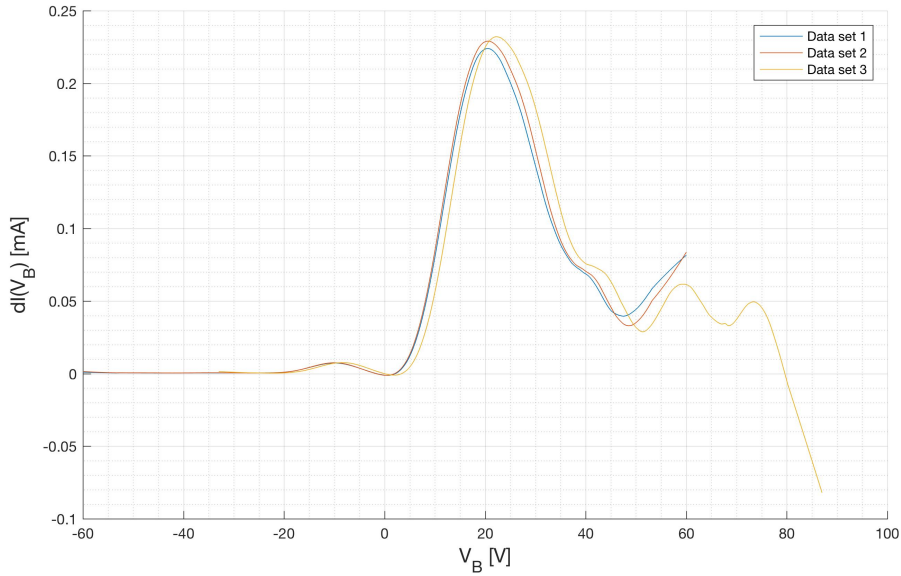


Figure 5.4:

is measuring the plasma potential of the accelerated ion beam, while the Langmuir probe is picking up the average, background plasma potential distributed by the more mobile electrons. As mentioned in section 4.2 only ions with a large enough parallel kinetic energy can pass through to the collector, i.e. ions flowing parallel with the ion beam from the source. All lower energy ions are being screened along with any ions with a different angle velocity vector, resulting in a small sample of high energy ions collected at a straight angle. The Langmuir probe however has an effective collection area that encompasses both sides of the planar probe, meaning it picks up particles from all directions and it also collects the electron saturation current, averaging the plasma potential from the whole chamber.

The plasma potentials seem to indicate the presence of an ion beam, which is what we want when using the chamber to simulate the the motion of a rocket or satellite with reference to the ionosphere. Further tests need to be done on this to properly determine the geometry of the plasma and the possible beam. Measurements should be made with a Langmuir probe at the position of the RFEA and vice versa, while also taking measurements with

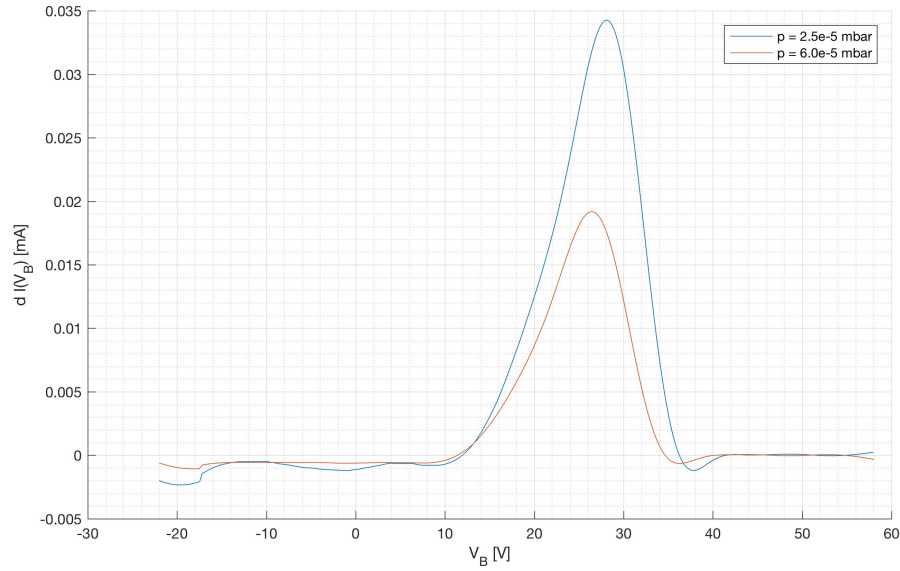


Figure 5.5: The first derivatives of two of the IV-curves from 5.3 at the indicated pressure values. This is known as the ion energy distribution

both probes at a 90 degree angle to the center axis of the chamber.

5.2.2 Electron temperature

The electron temperature T_e can be found from the slope of the semilogarithmic IV-curve in the region between the floating potential and the plasma potential, seen as region B in figure 4.1. Equation (4.5) or equation (4.6) is then applied to calculate the values of T_e in kelvin or electronvolts respectively. dV_B and $d(\ln I(V_B))$ is determined by two sets of coordinates, $[V_{B,1}, I(V_B)_1]$ and $[V_{B,2}, I(V_B)_2]$, found on each side of where the IV-curve is exponential, i.e. where the semilogarithmic IV-curve is approximately linear. To make sure we only get a contribution from the electron current, the ion saturation current $I_{sat,i}$ is subtracted from the data sets.

The IV-curves from figure 5.2 (minus $I_{sat,i}$) are displayed with a logarithmic y-axis in figure 5.6. The calculated values for the electron temperatures are listed in table 5.2.

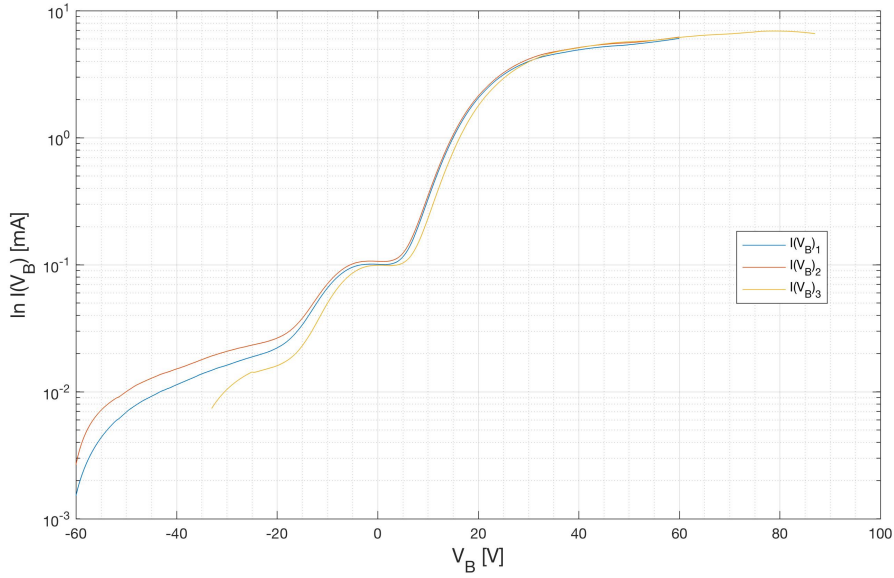


Figure 5.6: Characteristic IV-curve with a semilogarithmic y-axis.

Data set #	T_e [eV]
1	4.257
2	4.244
3	4.228

Table 5.2: Electron temperatures T_e for the three different data sets plotted in figure 5.6

The calculated values are very consistent and as expected, the electron temperature in plasma sources typically has a value between $2 - 5$ eV [14].

The electron temperature is closely related to the applied voltages and filament currents in the source [2]. In figure 5.7 values for the electron temperature was calculated using equation (4.6) for four different data sets sampled at different settings for the neutralizer current. Being able to vary the electron temperature in the plasma is very useful for simulating the ionosphere, depending on which altitude we are interested in.

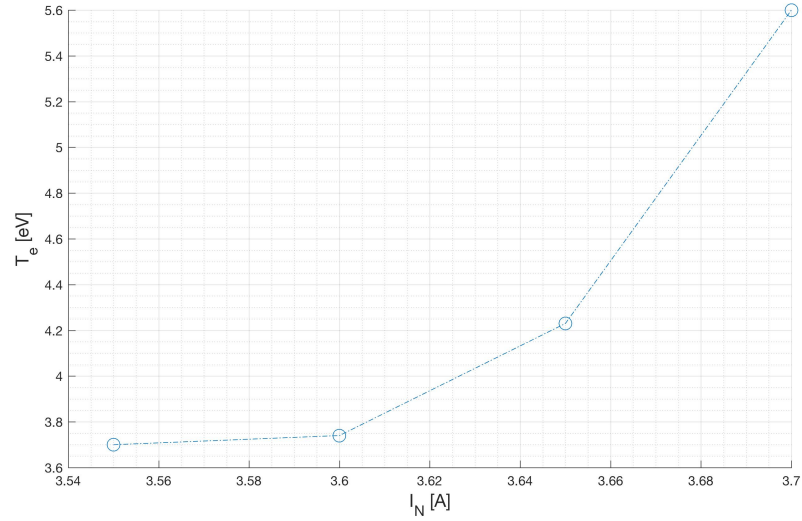


Figure 5.7: Electron temperature as a function of the neutralizing filament current.

5.2.3 Ion velocity

The ions collected by a probe are considered to have a velocity equal to the Bohm velocity, given in equation 2.14. Using the electron temperatures from section 5.2.2 and the argon mass $m_i = M_{Ar} = 39.948 u$ we find the ion velocity values for the Langmuir IV-characteristics presented in figure 5.2.

Data set #	v_B [m/s]
1	3204.32
2	3201.69
3	3195.65

Table 5.3: The calculated ion velocities at the sheath edge of the probe for the Langmuir IV-characteristics shown in figure 5.2.

5.2.4 Ion density

The ion saturation current collected by a probe is given by equation 4.1. For the Langmuir probe, A is the effective collecting area of the probe, which

we can approximate to the area of both sides of the planar probe, i.e. $A = 2\pi r^2 = 1.57 \text{ cm}^2$. We can assume this because the ions in our plasma are not magnetized (more on this in section 4.1.1). Using the data sets from figure 5.2, the ion saturation current values can be directly read from the measured data as the most negative value on the left hand side of the plot. We also use the values for the ion velocity found in section 5.2.3 and equation 4.2 with $q = -e$ to find the ion densities at the sheath edge for the Langmuir characteristics; listed in table 5.4.

Data set #	$I_{sat,i}$ [mA]	n_i [ions/cm ³]
1	-0.1470	$1.824 \cdot 10^{11}$
2	-0.1523	$1.891 \cdot 10^{11}$
3	-0.1454	$1.809 \cdot 10^{11}$

Table 5.4: Ion density at the sheath edge of the probe calculated from the Langmuir IV-characteristics shown in figure 5.2.

5.2.5 Electron density

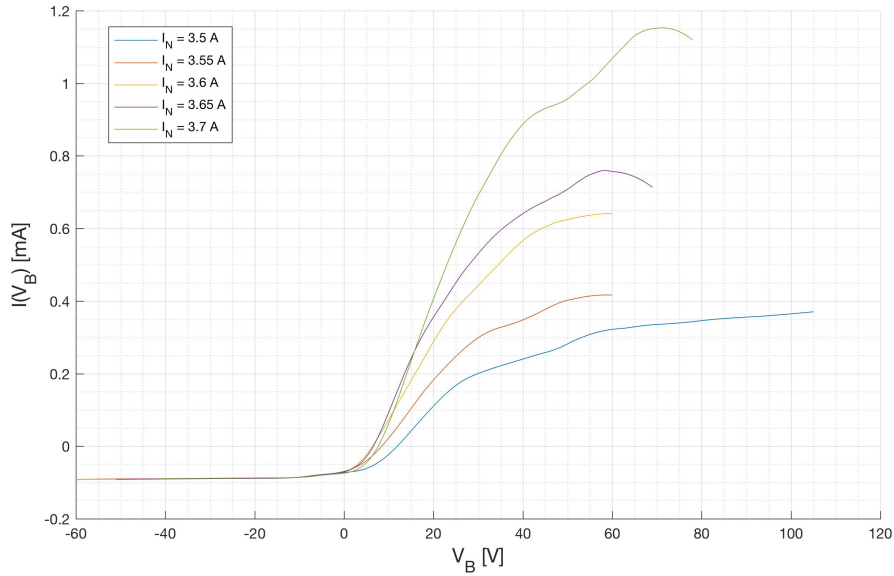


Figure 5.8: IV-characteristics with varied neutralizer current

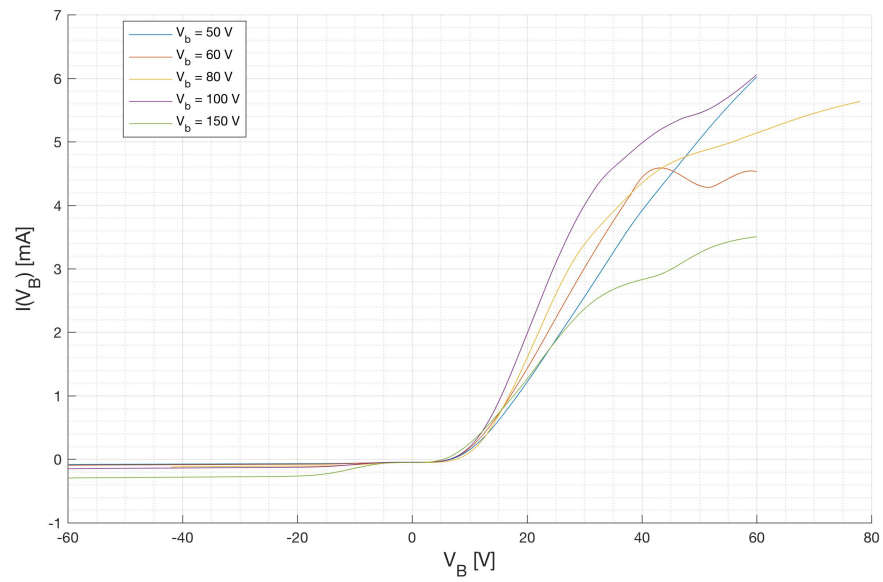


Figure 5.9: IV-characteristics with varied breakdown potential

Chapter 6

Conclusion and future work

The primary focus of this thesis was the installation and characterization of an electron bombardment type plasma source for a Space Simulation Chamber (SSC). The goal was that the chamber can be used to test satellite and sounding rocket instrumentation, thus be capable of producing ionospheric plasma conditions, along with an ion beam that can simulate the velocity of a rocket or satellite relative to the atmosphere. The plasma also needed to be reproductive.

The source was prepared for operation before it could be installed. This included changing the filaments and checking the conditions of the electrical connections and magnetic field. A new setup of power sources for the different components was also done. It was then installed and characterized in the Space Simulation Chamber. Some hang ups were encountered and solved.

Two different electrostatic probes were used to analyse the plasma. A basic Langmuir probe, useful for finding parameters like the plasma potential, electron temperature and plasma density, and a retarding field energy analyzer (RFEA) for finding the ion saturation current and ion energy distribution.

Some inconsistency was found in the plasma potential between the two probes, the plasma potential was higher further away from the source measured with the RFEA probe. This only measures ion energies, thus it may be

indicating the presence of an ion beam. The plasma density is in the order of 10^{11} cm^3 and the electron temperature is in the range 3-5 eV and can be varied using the neutralizing filament. The results are very reproducible.

Some work that naturally could follow this would be to create a program to control the voltage- and current sources, a suggestion is that it should follow the discharge current and adjust the filament currents continuously so I_U lies between 100-150 mA, which is the desired operational values. Map the whole chamber using moveable probes, along several axis and determine the geometry of the ion beam, and find the proper ion velocity.

Bibliography

- [1] Asgeir Brekke. *Physics of the Upper Polar Atmosphere (Second edition)*. Springer-Verlag Berlin Heidelberg, Tromsø, second edition, 2013.
- [2] Svein-Erik Hamran. *Simulering av Ionosfæreplasma*. Master thesis, Norges Tekniske Høyskole, 1984.
- [3] Farley and Hagfors. Berndraft TH. 1999.
- [4] K. Fang, K. I. Oyama, and C. Z. Cheng. Plasma measurements in the space plasma operation chamber (SPOC). *Chinese Journal of Physics*, 53(1):1–30, 2015.
- [5] W. K. Rehmann and N. H. Stone. The simulation of ionospheric conditions for space vehicles. 1970.
- [6] Kenneth Rein-Heggebakken, Gunnar Nielsen, and Tra Nguyen. *Konstruksjon av plasmakilde*. Thesis, Universitetet i Oslo, 2004.
- [7] Harold R. Kaufman, Paul D. Reader, and North Olmsted. Electrostatic ion rocket engine. *U.S. Patent*, 3,262,262, 1966.
- [8] Harold R. Kaufman. Electrostatic thrustors, 1964.
- [9] Harold R. Kaufman and Paul D. Reader. Electrostatic ion engine having a permanent magnetic circuit. *U.S. Patent*, 3,238,715, 1966.
- [10] Harold R. Kaufman, Raymond S. Robinson, and William E. Hughes. Electron Bombardment Ion Source. *U.S. Patent*, 4,481,062, 1984.
- [11] NASA Administrator. Glenn Contributions to Deep Space 1, 2015.

- [12] Horst W Loeb. Plasma-based ion beam sources. *Plasma Physics and Controlled Fusion*, 47(12B):B565–B576, 2005.
- [13] Harold R. Kaufman and Paul D. Reader. United States Patent. *U.S. Patent*, 3,956,666, 1976.
- [14] Michael A. Lieberman and Allan J. Lichtenberg. *Principles of Plasma Discharges and Materials Processing*. John Wiley & Sons, Inc., Hoboken, New Jersey, second edition, 2005.
- [15] J. Reece. Roth. *Industrial Plasma Engineering - Volume 1: Principles*. Institute of Physics Publishing Bristol and Philadelphia, 1995.
- [16] A Kramida, Yu Ralchenko, J Reader, and NIST ASD Team. NIST Atomic Spectra Database (ver. 5.3), [Online], 2014.
- [17] Harold R. Kaufman. Performance correlation for electron- bombardment ion sources. 1965.
- [18] Stéphane Mazouffre. Electric propulsion for satellites and spacecraft: established technologies and novel approaches. *Plasma Sources Science and Technology*, 25(3):033002, 2016.
- [19] Zoltán Donkó. Particle simulation methods for studies of low-pressure plasma sources. *Plasma Sources Science and Technology*, 20(2):024001, apr 2011.
- [20] K. T. A. L. Burm. Calculation of the Townsend Discharge Coefficients and the Paschen Curve Coefficients. *Contributions to Plasma Physics*, 47(3):177–182, may 2007.
- [21] J. M. Meek. A Theory of Spark Discharge. *Physical Review*, 57(8):722–728, apr 1940.
- [22] C. L. Wadhwa. *High voltage engineering*. New Age International, 2007.
- [23] G. Petraconi, H. S. Maciel, R. S. Pessoa, G. Murakami, M. Massi, C. Otani, W. M. I. Uruchi, and B.N. Sismanoglu. Longitudinal magnetic

- field effect on the electrical breakdown in low pressure gases. *Brazilian Journal of Physics*, 34(4b):1662–1666, dec 2004.
- [24] Fred. Theory - fusor.edu, 2016.
- [25] Harold R. Kaufman and Raymond S. Robinson. Ion source design for industrial applications. 1981.
- [26] J. L. Burch, Robert L. Carovillano, and Spiro K. Antiochos. *Sun-earth plasma connections*. American Geophysical Union, 1999.
- [27] Wilhelm and H. E. Theoretical investigations on plasma processes in the Kaufman thruster. Technical report, 1973.
- [28] Karianne Dyrland. FYS-3730 Project paper in Space Physics - Review of a plasma source for a Space Simulation Chamber (SSC). Technical report, 2015.
- [29] Jan-Roald Garden Huru. *Ny Plasmakilde For Simulering Av Ionosfæreplasma i Plasmasimuleringskammer*. Thesis, Høgskolen i Narvik, FFI, 2002.
- [30] Ulf-Peter Hoppe. Bidrag til ”Nasjonal Romforskningsgruppe” fra romfysikkgruppen på FFI. Technical report, FFI, 2010.
- [31] Kenneth Rein-Heggebakken. Functional Design Specifications for Konstruksjon av plasmakilde. Technical report, FFI, 2004.
- [32] Charles E. Wilkes, James W. Summers, Charles Anthony Daniels, and Mark T. Berard. *PVC Handbook*. Hanser, 2005.
- [33] E. et al Grønvoll. UiT FYS-3017 Lab exercise no.2: Langmuir analysis of IV characteristics. (1):1–19, 2015.
- [34] Irving Langmuir and H. M. Mott-Smith. The Theory of Collectors in Gaseous Discharges. *Physical Review*, 28(4):727–763, oct 1926.
- [35] V. A. Godyak, R. B. Piejak, and B. M. Alexandrovich. Probe diagnostics of non-Maxwellian plasmas. *Journal of Applied Physics*, 73(8):3657, 1993.

- [36] I. H. Hutchinson. The invalidity of a Mach probe model. *Physics of Plasmas*, 9(5):1832, 2002.
- [37] Ane Aanesland, Åshild Fredriksen, Hanne Sigrun Byhring, and Njål Gulbrandsen. UiT FYS-3017 Lab exercise no.4 - Diagnostics with the retarding field energy analyzer (RFEA). (3):1–10.
- [38] D. Gahan, B. Dolinaj, and M. B. Hopkins. Retarding field analyzer for ion energy distribution measurements at a radio-frequency biased electrode. *Review of Scientific Instruments*, 79(3):11–13, 2008.
- [39] N. Gulbrandsen, Åshild Fredriksen, J. Carr, and E. Scime. A comparison of ion beam measurements by retarding field energy analyzer and laser induced fluorescence in helicon plasma devices. *Physics of Plasmas*, 22(3), 2015.
- [40] Y. Cui, Y. Zou, A. Valfells, M. Reiser, M. Walter, I. Haber, R. A. Kishek, S. Bernal, and P. G. O’Shea. Design and operation of a retarding field energy analyzer with variable focusing for space-charge-dominated electron beams. *Review of Scientific Instruments*, 75(8):2736–2745, 2004.

